nature photonics

SUPPLEMENTARY INFORMATION

https://doi.org/10.1038/s41566-017-0079-y

In the format provided by the authors and unedited.

Far-field nanoscopy on a semiconductor quantum dot via a rapid-adiabatic-passage-based switch

Timo Kaldewey[1]*, Andreas V. Kuhlmann[1,3], Sascha R. Valentin[2], Arne Ludwig[2], Andreas D. Wieck[2] and Richard J. Warburton[1]

[1]Department of Physics, University of Basel, Basel, Switzerland. [2]Lehrstuhl für Angewandte Festkörperphysik, Ruhr-Universität Bochum, Bochum, Germany. Present address: [3]IBM Research-Zurich, Rüschlikon, Switzerland. *e-mail: timo.kaldewey@unibas.ch

Far-field nanoscopy on a semiconductor quantum dot via a rapid-adiabatic-passage-based switch

Supplementary Information

Timo Kaldewey,[1, a)] Andreas V. Kuhlmann,[1, b)] Sascha R. Valentin,[2] Arne Ludwig,[2] Andreas D. Wieck,[2] and Richard J. Warburton[1]

[1)] *Department of Physics, University of Basel, Basel, Switzerland*

[2)] *Lehrstuhl für Angewandte Festkörperphysik, Ruhr-Universität Bochum, Bochum, Germany*

(Dated: 18 December 2017)

I. SUPPLEMENTARY MATERIALS

A. The semiconductor sample

1. The heterostructure

The InGaAs quantum dots (QDs) are embedded in a GaAs n-i-p diode grown by molecular beam epitaxy[1]. The layer structure is shown in Fig. S1a. Initially, a superlattice (18 periods of a 2 nm GaAs, 2 nm AlAs unit) is grown on top of a GaAs wafer in order to smooth the wafer surface. Following this, a distributed Bragg reflector (DBR) consisting of 16 periods of 68.6 nm GaAs and 81.4 nm AlAs is grown in order to increase the photon collection efficiency from the top side. The back contact is provided by a layer of n-doped GaAs. An intrinsic region, 30 nm of GaAs, acts as tunnel barrier for the InGaAs QDs. The QDs are capped by 153 nm GaAs. A subsequent barrier (a superlattice consisting of 46 periods of a 3 nm AlAs, 1 nm GaAs unit) hinders current flow in the strong vertical electric field. The penultimate layer is p-doped GaAs forming the top contact of the diode. Compared to a Schottky diode structure the absorption of photons in the top gate is reduced. The final layer, 44 nm undoped GaAs, places the p-doped layer around a node-position of the standing electromagnetic wave. The n- and p-doped layers are contacted independently. Selective etching of the capping allows contacting of the buried p-layer. Access to the n-layer is provided by wet etching of a mesa structure around the solid immersion lens (SIL) [A.W.I. Industries, USA]. The n-contact is grounded; a voltage V_g is applied to the p-contact.

2. Quantum dot charging

The sample is probed at liquid helium temperature, 4.2 K, in a bath cryostat. At these temperatures, there is a pronounced Coulomb blockade: the number of electrons in the quantum dot changes step-wise as a function of V_g[2–4]. Fig. S1b shows the photoluminescence (PL) of a single QD as function of V_g. There are plateaus with emission from the neutral exciton, X^0, from the negatively charged trion (two-electron, one-hole complex), X^{1-}, and from the X^{2-}. There is also a much weaker PL signal from the positively charged trion, X^{1+}, at the most negative V_g. The X^0 is used in the imaging experiments. We note that the V_g-overlap of the X^0-X^{1-} plateau is not a feature once the QD is driven with resonant excitation[5].

3. Resonance fluorescence detection: CW excitation

Resonance fluorescence (RF), the scattering induced by resonant excitation, is shown in Fig. S1c on the X^0 transition. The laser excitation and the detection are orthogonally polarized in order to suppress reflected laser light in the detection channel: this is a polarization-based dark-field technique[6,7]. With our RF multi-purpose microscope (described in sec. I B 2), CW excitation, and a zirconia SIL on the sample surface, we reach a driving laser extinction ratio of 10^7:1 and a collection efficiency of approximately $5-10\%$. The net result is that the signal:background ratio is 250:1, e.g. Fig. S1c. The X^0 transition is split into two lines, Fig. S1c, as a consequence of the fine structure splitting, FSS (see Fig. 1 of the main article). The linewidths are around 2 μeV, approximately 2.5 times larger than the transform limit[6]. Above saturation, the RF is more than 5 MHz corresponding to a single photon flux of 25 MHz. The detector, a silicon single photon avalanche diode (SPAD), has a quantum efficiency of 20% at a wavelength of 950 nm.

B. The experiment

The imaging experiment consists of a laser system and a cryogenic optical microscope, Fig. S2. The laser is a tunable, mode-locked Ti:sapphire [Coherent, Mira900] which creates close-to-transform-limited pulses with a pulse duration of ~100 fs. The pulse train is expanded with a beam expander and split into two. The individual pulse trains are directed into homebuilt, compact pulse shaper units (PS1, PS2) which introduce chirp by introducing a wavelength dependent phase shift. Subse-

a)Electronic mail: timo.kaldewey@unibas.ch
b)current address: IBM Research-Zurich, Rüschlikon, Switzerland

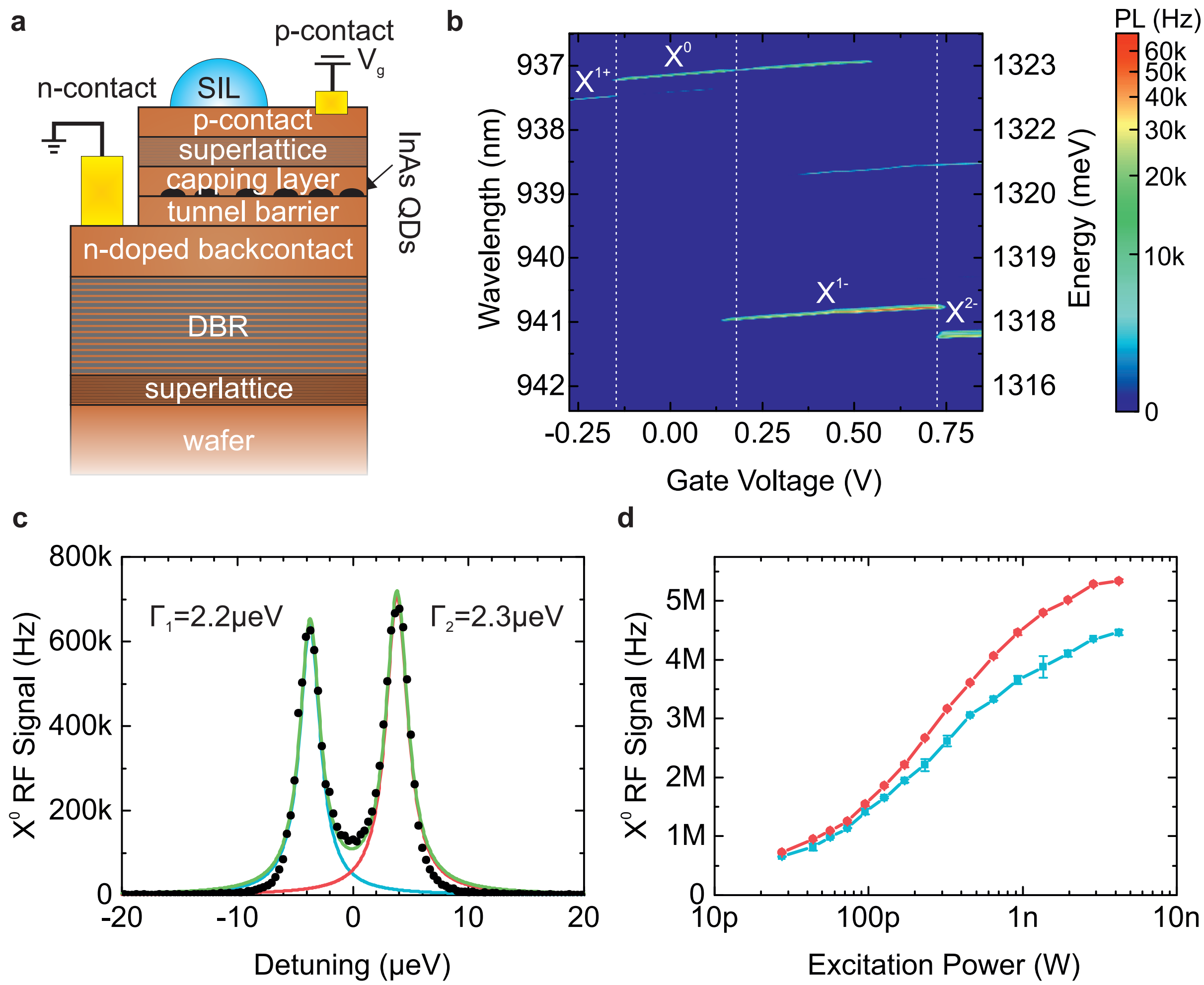

FIG. S1. **Resonance fluorescence on a single quantum dot (QD): CW excitation.** **(a)** The heterostructure: InGaAs QDs in an n-i-p diode with weak cavity structure. In the growth direction: GaAs wafer, GaAs/AlAs superlattice (18 periods), distributed Bragg reflector (DBR) consisting of 16 GaAs/AlAs pairs, Si doped GaAs back contact, GaAs tunnel barrier, InGaAs QDs, capping layer, blocking barrier consisting of AlAs/GaAs superlattice, C-doped GaAs as top contact. A ZrO_2 solid immersion lens (SIL) is placed on the sample surface to increase the photon extraction efficiency. **(b)** Photoluminescence of a single QD, QD01, as a function of applied gate voltage and emission wavelength. The QD was excited non-resonantly at 830 nm with a power of 17 μW. **(c)** Resonance fluorescence spectrum of QD01 X^0 with resonant, circularly polarized excitation of 27 pW. The data (black circles) were fitted with a sum of two Lorentzian functions (green, individual functions shown in red and blue). The individual linewidths are 2.2 μeV and 2.3 μeV. The photons were detected with a silicon single photon avalanche diode with an integration time of 5 ms. The laser frequency was 319.778 62 THz (wavelength 937.530 nm). **(d)** Fitted amplitudes of resonance fluorescence as a function of excitation power for the two X^0 transitions.

quently, one pulse is delayed with respect to the other in a 300 mm delay line [Zaber, A-LSQ300A-E01], leading to a delay of up to 2 ns, and then power and polarization are controlled (neutral density filters for coarse power control; a half-wave plate, polariser, half-wave plate combination for fine power control and control of the linear polarization axis). Finally, the two pulse trains are coupled into separate single-mode optical fibres.

The microscope consists of the "head" at room temperature and an objective lens plus nano-positioners [attocube systems, ANPx101 and ANPz101] at low temperature, Fig. S2. The nano-positioners allow the sample to be positioned at the focus of the microscope, and images to be recorded by sample scanning [attocube systems, ANSxyz100/LT]. The head converts one pulse train into a collimated beam with a lateral Gaussian intensity profile, the other into a collimated beam also with a lateral Gaussian intensity profile but azimuthal phase dependence. The two pulse trains are focused by the objective onto the sample with close-to-diffraction-limited performance. The objective cuts the beams only in the wings of the Gaussian profile resulting in a Gauss-shaped focus and a doughnut-shaped focus. Resonance fluorescence is collected by the same objective and coupled in the microscope head into a third fibre which transports the signal to the detector, either a spectrometer-CCD camera sys-

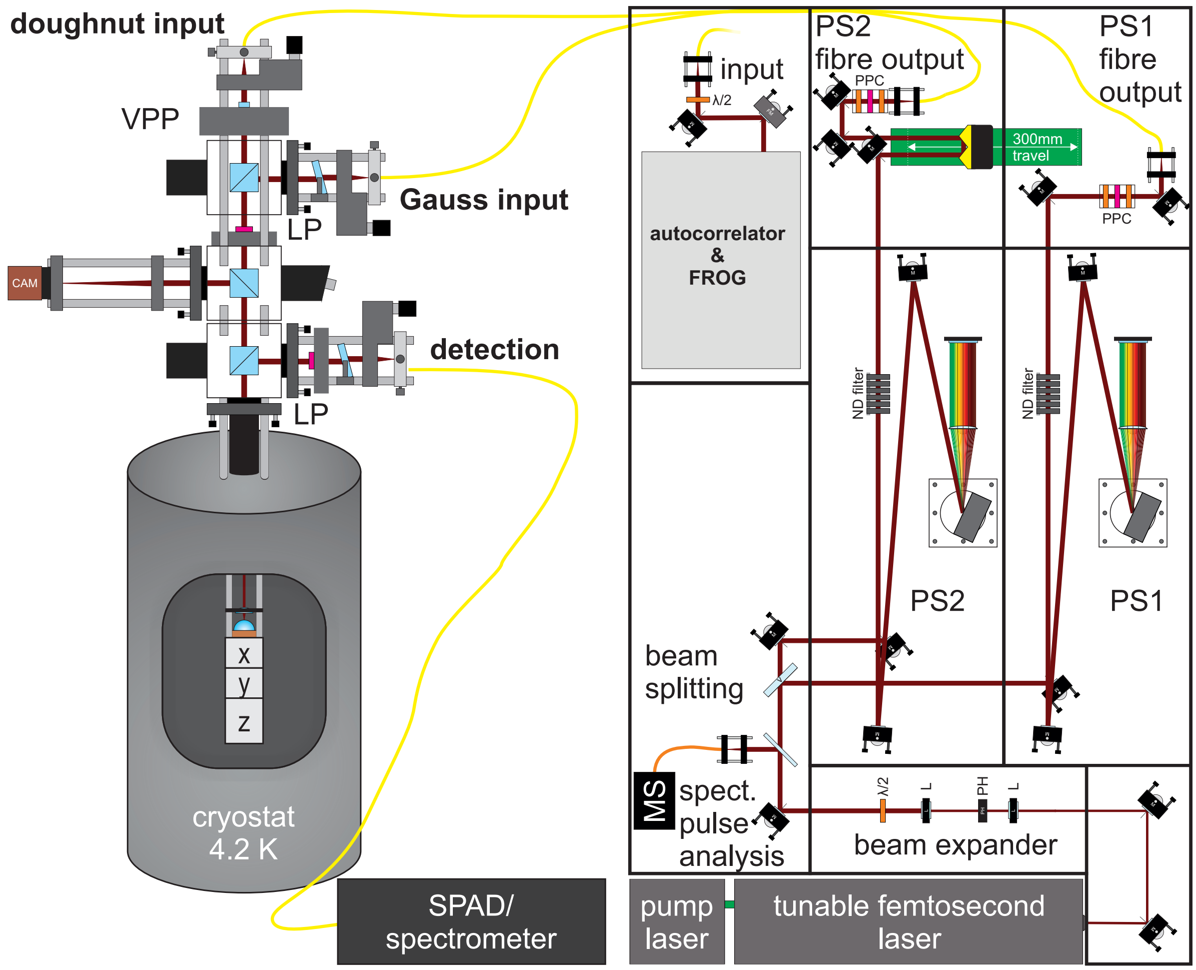

FIG. S2. **Scheme of the whole experiment.** L lens, $\lambda/2$ half-wave plate, PH pin-hole, MS mini-spectrometer, PS pulse shaper, ND neutral density filter, PPC power-polarization-control, FROG frequency-resolved-optical-gating, VPP vortex phase-plate, LP linear polariser, SPAD single photon avalanche diode. The autocorrelator-FROG combination is used to characterise the pulses before the microscope and after the glass fibre.

tem [Princeton Instruments, Acton SP2500] or a SPAD [PicoQuant, Tau-Spad 20].

1. Creation and characterization of chirped pulses

A controlled chirp is introduced into the laser pulses using a compact, folded $4f$-pulse shaper[8], Fig. S3b. Our scheme retains all the frequency components of the femto-second laser. Introducing chirp inevitably results in an increased pulse duration.

An unchirped pulse is directed onto a grating and its first order diffraction is then focused by a cylindrical lens onto a mirror. The lens and mirror are mounted together on a platform which can be moved with respect to the grating with a micrometer linear stage, Fig. S3b. This allows a variation of the lens–grating separation while keeping the mirror in the focal plane of the lens. A lens–grating separation larger than the focal length (positive displacement) introduces a negative chirp, a separation smaller than the focal length (negative displacement) results in a positive chirp[9]. Autocorrelation measurements of the shaped pulses show that the intensity of the pulses are extremely well described by a Gaussian function of time. We demonstrate in Fig. S3b a stretching of the original, transform-limited 130 fs pulses to a duration of more than 10 ps, an increase by a factor of 100.

The pulse duration is linked to the chirp. The electric field of the unchirped pulse can be described with a Gaussian envelope in the time domain:

$$\begin{aligned} E(t) =& E_0 \exp\left(\frac{-t^2}{2\tau_0^2} - i\omega_0 t\right) \\ \Delta t^I_{0,\mathrm{FWHM}} =& 2\sqrt{\ln 2}\,\tau_0 \end{aligned}$$

where $\Delta t^I_{0,\mathrm{FWHM}}$ is the full-width-at-half-maximum (FWHM) of the pulse intensity. $\Delta t^I_{0,\mathrm{FWHM}} = 130\,\mathrm{fs}$ here. Equivalently, the unchirped pulse can be described in the

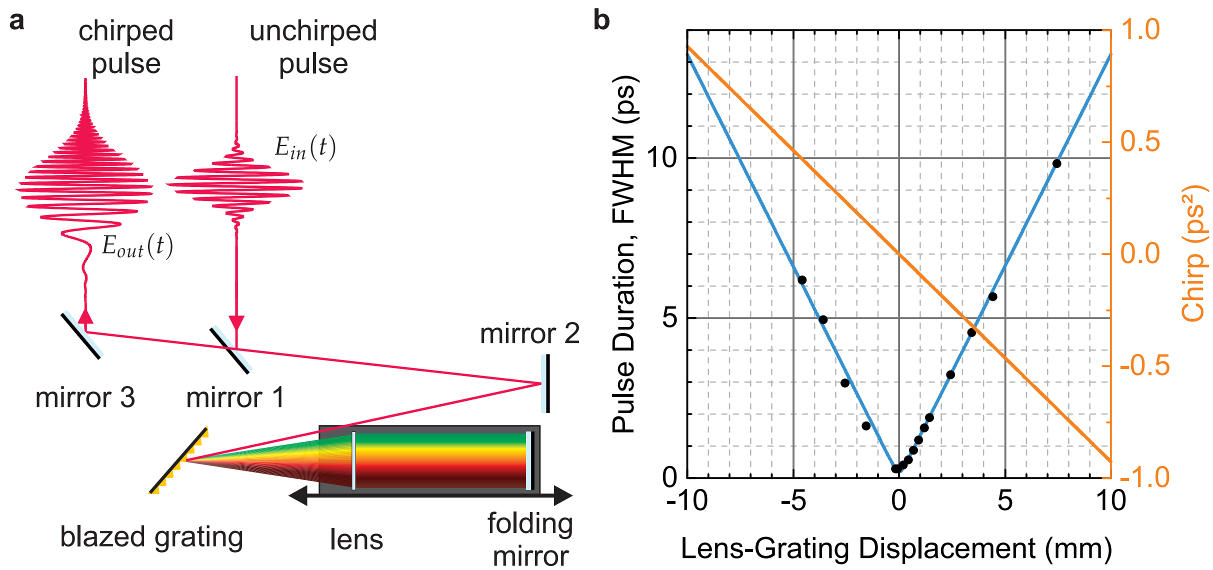

FIG. S3. **Compact pulse shaper: concept and performance. (a)** The incident beam is directed with mirrors 1 and 2 onto a blazed grating (1,800 lines/mm), diffracted and then focused by a cylindrical lens (focal length 150 mm) onto a mirror placed in the focal plane of the lens. The lens and the folding mirror are mounted on a moving platform. A displacement (up to ±10 mm) between grating and lens–mirror assembly introduces chirp. Note that the beam is reflected slightly upwards by the mirror in the pulse shaper such that it overshoots mirror 1 on the return path. **(b)** Pulse duration Δt^I_{FWHM} as a function of the lens–grating displacement. The pulse duration was measured with a FROG autocorrelator. The measured data points (black circles) are fitted (blue solid line) using the result for quadratic phase, eq. 2b. The sweep rate α calculated from the pulse duration is shown on the right axis.

frequency domain:

$$\begin{aligned} E(\omega) =& E_0\tau^2 \exp\left[-\frac{\tau_0^2}{2}(\omega-\omega_0)^2\right] \\ \Delta\omega^I_{0,\text{FWHM}} =& \frac{2\sqrt{\ln 2}}{\tau_0}. \end{aligned}$$

The role of the pulse shaper is to add a phase for each frequency component:

$$\phi(\omega) = \phi_0 + \phi_1(\omega-\omega_0) + \frac{\phi_2}{2}(\omega-\omega_0)^2. \tag{1}$$

The linear phase term shifts the entire pulse in time and is irrelevant here; the quadratic term represents a chirp. In practice, ϕ_2 is directly proportional to the displacement of the pulse shaper[10]. The link between ϕ_2 and the new pulse duration τ is:

$$\tau = \sqrt{\tau_0^2 + \left(\frac{\phi_2}{\tau_0}\right)^2} \tag{2a}$$

$$\Delta t^I_{\text{FWHM}} = \sqrt{\left(\Delta t^I_{0,\text{FWHM}}\right)^2 + \left(\frac{\phi_2\ 4\ln 2}{\Delta t^I_{0,\text{FWHM}}}\right)^2}. \tag{2b}$$

A key parameter for adiabatic passage is the sweep rate α. It is related to ϕ_2 by

$$\frac{\mathrm{d}}{\mathrm{d}t}\omega(t) = \alpha = \frac{\phi_2}{\tau_0^4+\phi_2^2}. \tag{3}$$

We work here in the regime $\phi_2 \gg \tau_0^2$ such that $\tau \simeq \phi_0/\tau_0$ and $\alpha \simeq 1/\phi_2$.

The measured pulse duration as a function of displacement is shown in Fig. S3b. The results can be described perfectly with a quadratic phase dependence, eq. 1, allowing us to determine the sweep rate from eq. 3. Our pulse shaper is capable of generating ϕ_2 up to a few ps^2 with both signs. With a transform limited pulse duration of 130 fs and a chirp range 0 ps^2 to 1 ps^2 we can reach sweep rates from 1 ps^{-2} to 80 ps^{-2}. We note that the 8 m long single mode fibres used to transport the laser pulses to the microscope in our experiment, Fig. S2, introduce a positive chirp of 0.3 ± 0.1 ps^2: this is compensated with our pulse shaper.

2. Microscope design

The microscope is based on a former version of an RF confocal microscope[7]. The "head", Fig. S4, accepts two fibre inputs. In each input, the exact propagation axis is controlled (by rotating a laser window and a tilt stage) and a linear polarization state created (by a high quality polariser [Thorlabs, LPVIS050-MP]) after the two beams are combined by a beam-splitter and sent to the objective at low temperature. One input passes through a 2π vortex phase-plate (VPP) [RPC Photonics, VPP-1a]. The VPP introduces a phase shift to the wavefront: the phase shift is equal to the in-plane radial angle. On focusing, a

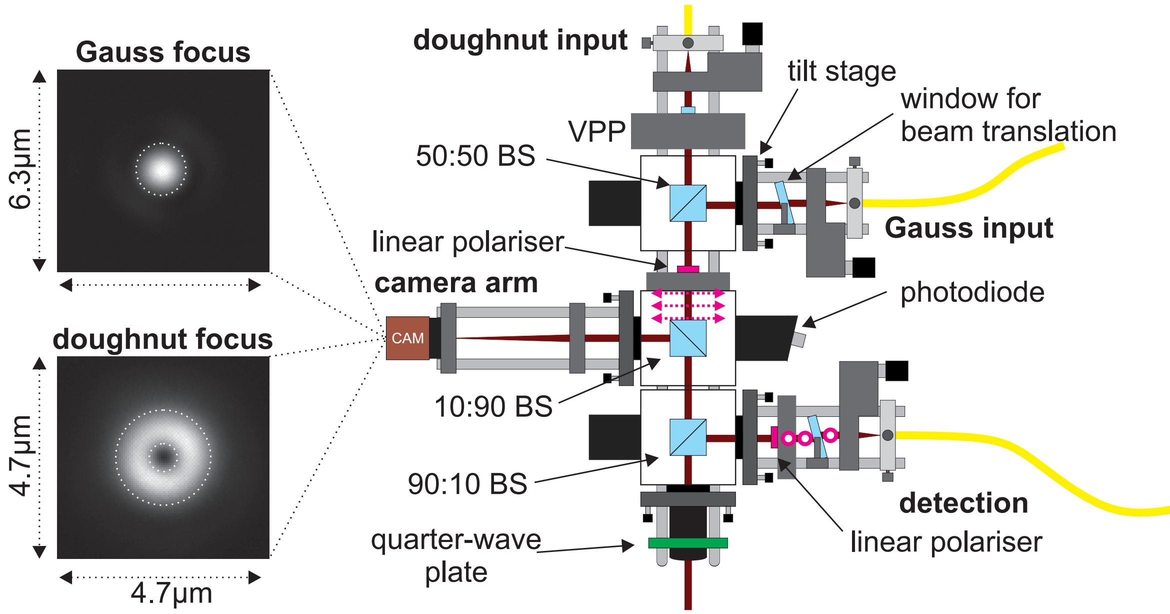

FIG. S4. **Microscope optics.** CAM camera, BS beam-splitter, VPP vortex phase plate.

doughnut intensity profile results. The fibre output collects the back-scattered signal. A camera [Allied Vision, Guppy Pro F-503]) provides an *in situ* image: it assists in positioning the sample surface with respect to the focus, and in co-aligning the three beams (two inputs, one output). The objective is a single element aspheric lens with numerical aperture $\mathrm{NA_O} = 0.68$ [Thorlabs, C330TME-B] which, with CW laser input, can operate at close to the diffraction limit at these wavelengths.

Reflected laser light is suppressed by exciting and detecting in orthogonal polarizations, either in a linear polarization basis as in previous experiments[6,7], or, as a new feature here, in a circular basis. We can make this choice by choosing the angle of a quarter wave-plate through which all beams pass, inserted as the final component in the microscope head. The extinction factor for the reflected laser light depends strongly on the quality of the focal spot. On a bare piece of GaAs we typically reach extinction ratios of 10^8:1; under a SIL on GaAs with CW excitation we reached in this experiment 10^7:1; and with excitation pulses, the single element aspheric lens, and a SIL on GaAs, the ratio decreases to 10^5:1. The performance worsens with pulsed excitation because of the spectral bandwidth of the laser pulses: the aspheric lens introduces a slight chromatic aberration.

The quality of the microscope's focus is tested by imaging a chrome grid with confocal detection in reflection. In this case, the overall resolution is determined by the point spread function (PSF) of the excitation (here Gaussian) folded with the PSF of the collection (here Gaussian also). With femto-second laser pulses with centre wavelength $\lambda = 940\,\mathrm{nm}$, we measured in this test experiment $\Delta x = 388 \pm 3\,\mathrm{nm}$ which is close to the diffraction limit. The intensity distribution as a function of lateral coordinates (x, y) in the focal plane is well described by a Gaussian (and not an Airy function). This is as expected: the laser pulses are transmitted to the optical microscope via an optical fibre, resulting in a Gaussian spatial intensity profile. On focussing, the objective cuts the beam only in the wings of the Gaussian profile resulting in a close-to-Gaussian spatial intensity profile in the focal plane: any Airy rings are very weak.

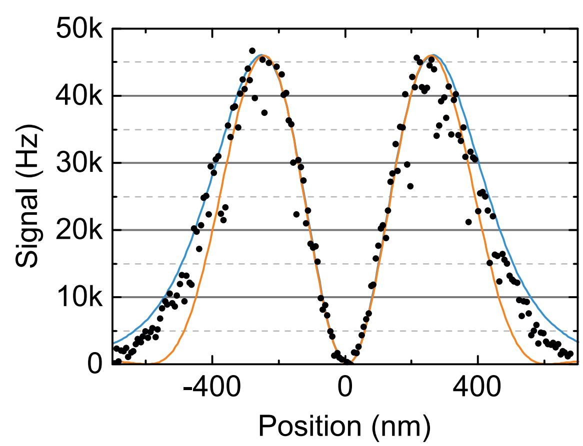

FIG. S5. **Quality of the doughnut focus.** The doughnut-shaped focus was measured with a quantum dot and left circularly polarized excitation, data points (black circles) are taken from the white dashed line in Fig. S10. Also shown are calculated foci for a Gaussian (blue solid line) and plane wave (orange solid line) incident on the objective, $|E_\mathrm{D}|^2$ with E_D from eq. 4b. Parameters for the calculation are $\lambda = 940\,\mathrm{nm}$, $n_\mathrm{SIL} = 2.13$, $\Delta X_{I,\mathrm{FWHM}} = 2.0\,\mathrm{mm}$ ($\sigma = 1.2\,\mathrm{mm}$), $f = 5.9\,\mathrm{mm}$.

The quality of the microscope's focus can also be tested

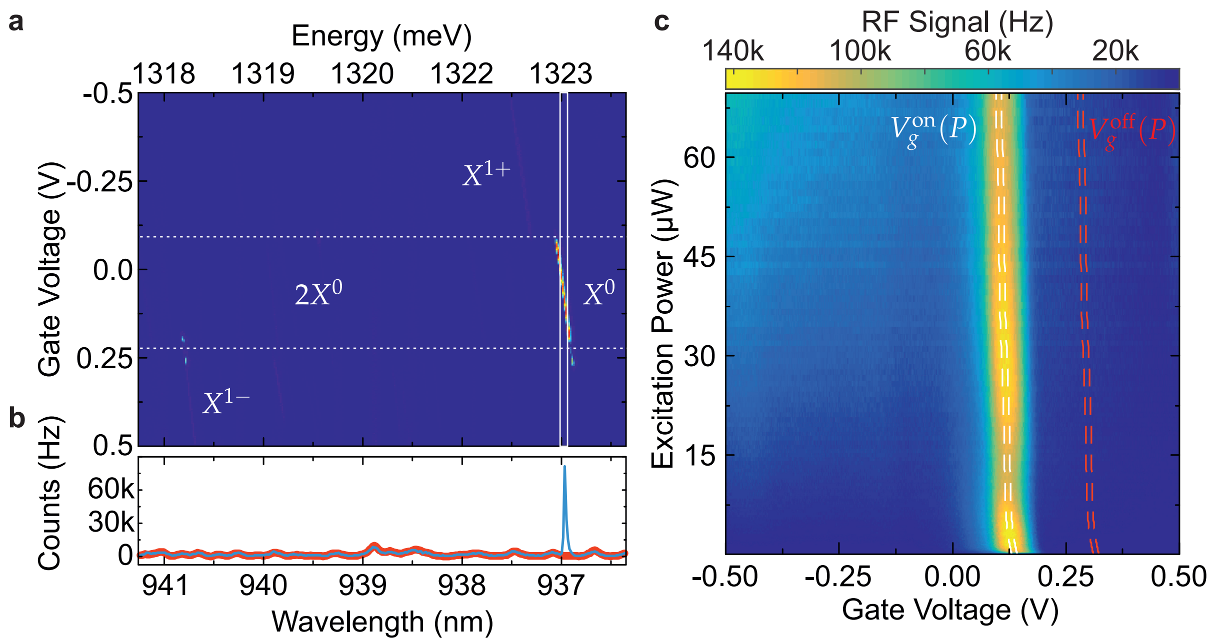

FIG. S6. **Resonance fluorescence (RF) on a single quantum dot: pulsed excitation.** RF with positively chirped excitation pulses with a spectral and temporal width of $\Delta\lambda^I_{\rm FWHM} = 9.70 \pm 0.30$ nm and $\Delta t^I_{\rm FWHM} = 7.0 \pm 0.3$ ps, respectively. The polarization was right circular, the integration time per spectrum 25 ms. **(a)** Signal following background subtraction (see b) as a function of applied gate voltage V_g and detection wavelength for an excitation power of 0.36 µW. The detection of RF from X^{1-}, X^{1+} and $2X^0$ after circularly polarized excitation is weak due to the cross polarized dark-field technique and the selection rules. **(b)** Signal versus wavelength: raw data at $V_g = 120$ mV (blue line). The laser background is determined from the whole dataset in (a): for every wavelength, the V_g with the smallest count rate is determined and this count rate is used to construct the laser background spectrum (red curve). Note that the laser suppression function is a quadratic function of wavelength about the alignment wavelength, superimposed with interference fringes. **(c)** Spectrally integrated RF from the white solid rectangle in (a) as a function of excitation power P and gate voltage. The final signal is the difference between the signal on the white dashed path, $V_g^{\rm on}(P)$, and the remaining background on the red dashed path, $V_g^{\rm off}(P)$.

in situ by using rapid adiabatic passage (RAP) on a single quantum dot. In this case (main article, Fig. 3d,e), we find $\Delta x = 587$ nm and $\Delta y = 563$ nm. This is entirely consistent with the confocal result. On imaging a quantum dot with a single, chirped pulse, the response is not a linear function of the excitation. With a Gaussian spatial profile, the quantum dot response is constant in the centre of the beam (where the intensities are high enough to invert the system using RAP), falling rapidly in the wings of the beam (where the intensities are too small to invert the system using RAP). In the simplified picture of a switch, the quantum dot response as a function of position is a step function. At high power, the step from "on" to "off" occurs far away from the central maximum. In this limit, the overall resolution is determined by the PSF of the collection only. Imaging a quantum dot with a single, intense chirped pulse we therefore expect a resolution of $\simeq 388 \times \sqrt{2} = 550$ nm. This is close to the measured values.

The quality of the doughnut-shaped focus is crucial for the imaging experiment: a low quality reduces the intensity of the central bright spot. We define quality here as the intensity ratio of the doughnut's maximum to its minimum: it quantifies the relative residual intensity in the centre, Fig. S5. Measured on a QD with left circularly polarized excitation, we reached values of 1200:1, a factor of about five higher than in right circularly polarized excitation. The dependence of the quality on the helicity of the polarization (with respect to the VPP) is in agreement with vector-field calculations[11] and reported experimental results on fluorescent nanoparticles[12]. With the correct choice of the helicity the residual intensity at the centre is very small in this experiment[12,13].

The microscope is simple to operate and robust: once aligned it remains aligned over several days.

3. Resonance fluorescence detection: pulsed excitation

The femto-second pulses are spectrally broad: they contain the frequencies to excite not just the neutral exciton, X^0, but also the biexciton, $2X^0$ and the trions, X^{1-} and X^{1+}, should the ultra-short laser pulses disrupt the Coulomb blockade. These concerns turn out to be unfounded. With a circularly polarized pulsed excitation, the RF from a single quantum dot lies almost entirely at the X^0 emission frequency, Fig. S6. The shift in emission frequency as a function of V_g reflects the dc Stark effect.

For chirped excitation with sufficient intensity to invert the system, equivalently for a π pulse with unchirped excitation, the RF:background ratio is $11:1$. At higher laser power, the background rises but the signal does not and the background signal dominates. We deal with this in two ways. First, the laser background is spectrally broad, the RF spectrally narrow, 5,000-times narrower in fact. We therefore collect the signal in a small spectral "window", typically a sub-nanometer wavelength extent. We do this simply by reading out the appropriate pixels on the CCD camera. In this way, only the laser background in a narrow bandwidth adds to the signal. Secondly, we measure the remaining laser background by recording the signal when the quantum dot is turned off. We implement this by recording a signal at two different values of V_g: $V_g^{\rm on}$ and $V_g^{\rm off}$. This is a simple modulation technique and is robust with respect to any changes in the performance of the microscope. The only complication in this procedure is a slight shift of $V_g^{\rm on}$ as a function of excitation power: this arises because a small amount of space charge is trapped in the device and shifts the X^0 resonance. Since the excitation power is constant during a scan in the imaging experiment, here the simple modulation technique is sufficient. Other experiments (main paper, Fig. 2c) are performed as a function of pulse area. We therefore record in this case the signal-plus-background in a small gate voltage range around the X^0 resonance. The signal is then extracted from a path following the slight shift of the resonance; the background is determined from the same dataset and the same path but shifted in V_g with respect to the resonance, Fig. S6c. This procedure enables us to determine the RF signal even at very large laser powers, corresponding to a pulse area up to 11π. The laser background contributes additional shot noise to the noise in the RF signal; there is also a systematic error which we estimate to be 20% of the signal at the highest laser powers, arising from weak interference effects of the two pulses in the imaging experiment and from a slight dependence in the choice of X^0 spectral bandwidth.

C. Imaging of two-level system with adiabatic passage: model

We construct a simple model of nanoscopic imaging of a quantum mechanical two-level system. The aim is to capture the essential features and to generate analytical results.

1. The optical fields: scalar theory

We calculate the field distribution in the focal plane using scalar diffraction theory applied to Gaussian beams. Strictly speaking, at high numerical apertures a full vector theory is required; additionally the beams are truncated Gaussians, truncated by the aperture of the ob-

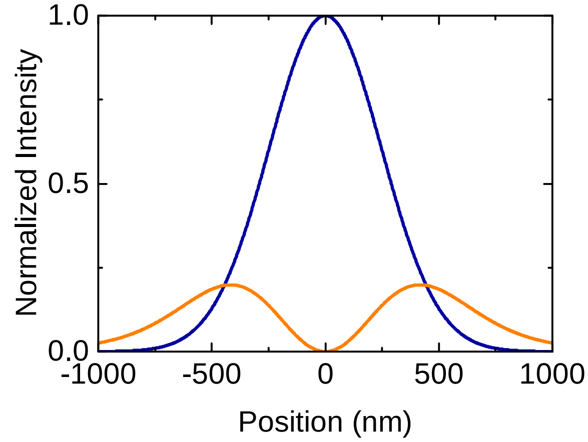

FIG. S7. **Gauss and doughnut intensity distributions.** $|E_{\rm G}(x,y=0)|^2$ and $|E_{\rm D}(x,y=0)|^2$ in eq. 4 are plotted with $E_{\rm G}^0 = E_{\rm D}^0 = 1$ in blue and orange, respectively. Parameters for the calculation are $\lambda = 940\,$nm, $n_{\rm SIL} = 2.13$, $\Delta X_{I,\rm FWHM} = 2.0\,$mm ($\sigma = 1.2\,$mm), $f = 5.9\,$mm.

jective lens. Extending the calculation to arbitrary input beams with a full vector theory is not difficult. The present approach has the virtue of simplicity.

In scalar theory, the electric field in the focal plane has the same polarization as the input polarization. The spatial distribution of the electric field in the focal plane is proportional to the Fourier transform of the (normalized) aperture function, $A(R,\phi)$, where (R,ϕ) are the radial coordinates in the plane of the aperture. For the Gaussian and doughnut beams

$$A_{\rm G}(R,\phi) = \frac{1}{2\pi\sigma^2}\exp\left(-\frac{R^2}{2\sigma^2}\right)$$
$$A_{\rm D}(R,\phi) = A_{\rm G}(R,\phi)\, e^{i\phi}$$

where σ describes the spatial extent of the beams before the focusing, $\Delta X_{I,\rm FWHM} = 2\sqrt{\ln 2}\,\sigma$. The fields in the focal plane (x,y) are given by

$$E_{\rm G}(r) = E_{\rm G}^0 \int_{R=0}^{\infty}\int_{\phi=0}^{2\pi} A_{\rm G}\exp\left(-ik\frac{r}{f}R\cos\phi\right) R\,{\rm d}R\,{\rm d}\phi$$
$$E_{\rm D}(r) = E_{\rm D}^0 \int_{R=0}^{\infty}\int_{\phi=0}^{2\pi} A_{\rm D}\exp\left(-ik\frac{r}{f}R\cos\phi\right) R\,{\rm d}R\,{\rm d}\phi$$

where $r = \sqrt{x^2+y^2}$ is the radial coordinate in the focal plane, $k = 2\pi/(\lambda/n_{\rm SIL})$, f is the focal length of the lens, and $E_{\rm G}^0$ ($E_{\rm D}^0$) is the amplitude of the Gauss (doughnut) beam.

$$E_{\rm G}(r) = E_{\rm G}^0\exp\left(-\frac{k^2\sigma^2 r^2}{2f^2}\right) \tag{4a}$$
$$E_{\rm D}(r) = E_{\rm D}^0\, i\frac{\sqrt{\pi}}{2\sqrt{2}}\frac{k\sigma r}{f}\exp\left(-\frac{k^2\sigma^2 r^2}{4f^2}\right) \cdot\left[I_0\left(\frac{k^2 r^2\sigma^2}{4f^2}\right) - I_1\left(\frac{k^2 r^2\sigma^2}{4f^2}\right)\right]. \tag{4b}$$

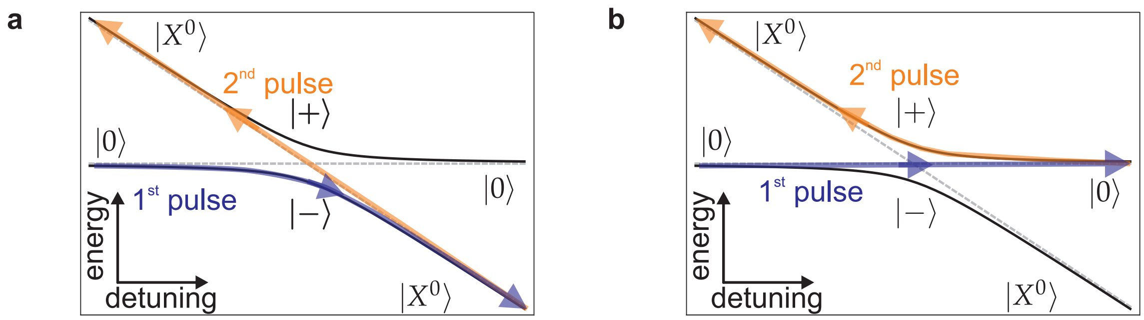

FIG. S8. **Two-pulse adiabatic passage on a two-level system.** The eigenenergies are plotted as a function of detuning. Two possible paths, a and b, show the two routes by which the system starts in the lower state $|0\rangle$ and ends up in the upper state $|1\rangle$ after a two pulse sequence. **(a)** Adiabatic passage followed by tunnelling; **(b)** tunnelling followed by adiabatic passage.

I_0 and I_1 are Bessel functions of the first kind with order 0 and 1, respectively. $E_\mathrm{G}(x, y)$ and $E_\mathrm{D}(x, y)$ are functions of (x, y) and have a Gaussian and a doughnut shape, respectively. The corresponding intensity distributions are depicted in Fig. S7. The FWHM of the Gaussian intensity distribution is $\Delta x_{I,\mathrm{FWHM}} = 2\sqrt{\ln 2}\ f/(k\sigma)$. $E_\mathrm{D}(r)$ is zero at $r = 0$.

2. Adiabatic passage: the Landau–Zener model

The case of a driven two-level system with time-dependent detuning was considered a long time ago by Landau[14] and by Zener[15]. Initially, the system is in one of the basis states, $|0\rangle$ or $|1\rangle$, and the detuning of the drive is large and negative. The detuning is then increased at a fixed rate passing through zero until it is large and positive. As a function of detuning, there is an avoided crossing in the eigenvalues, Fig. S8. The probability that the system makes a transition from one basis state to the other is given by one minus the Landau–Zener factor, p_LZ:

$$p_\mathrm{LZ}(\Omega, \alpha) = \exp\left(-\frac{\pi\Omega^2}{2\,|\alpha|}\right) \tag{5}$$

where Ω is the angular Rabi frequency, α the sweep rate (rate of change of the angular frequency). Here, the coupling arises from the interaction of the optical dipole μ_{01} with the electric field of the light wave, $\hbar\Omega = \mu_{01}E$. In the "sudden" regime when $p_\mathrm{LZ} \simeq 1$, the system "tunnels" through the avoided crossing and $|0\rangle \to |0\rangle$, $|1\rangle \to |1\rangle$. Alternatively, in the limit when $p_\mathrm{LZ} \ll 1$, the states are swapped $|0\rangle \to |1\rangle$, $|1\rangle \to |0\rangle$: this is adiabatic passage, Fig. S8. The imaging protocol exploits the exponential dependence of $p_\mathrm{LZ}(\Omega, \alpha)$ on Ω for fixed α: there is a "fast" transition from the sudden regime to the adiabatic passage regime as Ω increases.

In our case here, the excitation is not just chirped but also pulsed. In other words, Ω is a function of time which is not a feature of the Landau–Zener model. However, the Landau–Zener model captures the essential physics. The Rabi energies are at most a few meV in these experiments yet the spectral bandwidth of the pulse is ~ 15 meV. The peak of the laser spectrum is chosen to lie close to the X^0 transition. This means that in the region of the avoided crossing, the Rabi frequency is approximately constant in time, such that the Landau–Zener model is a reasonable one to describe the experiment. Of course, it is possible to integrate the Schrödinger equation over the pulse[16]. The advantage of the Landau–Zener model is that there is a simple analytical result.

The imaging experiment depends on the response to two pulses, the Gauss-pulse (Rabi coupling Ω_G, chirp α_G) and the doughnut-pulse (Rabi coupling Ω_D, chirp α_D). Ω_G and Ω_D depend on the lateral coordinates (x, y) in the focal plane: this enables imaging. In practice, $\alpha_\mathrm{G} > 0$, $\alpha_\mathrm{D} = -\alpha_\mathrm{G}$. The system is initially in the ground state, $|0\rangle$. There are two possible routes for the system to end up in the excited state, $|1\rangle$, Fig. S8. (In practice in the experiment, $|1\rangle \equiv |\mathrm{X}^0\rangle$.) Adding together the probabilities, the probability of occupying state $|1\rangle$ with the two-pulse combination is

$$\begin{aligned} P_1(\Omega_\mathrm{G}, \alpha_\mathrm{G}, \Omega_\mathrm{D}, \alpha_\mathrm{D}) = \ & p_\mathrm{LZ}(\Omega_\mathrm{G}, \alpha_\mathrm{G}) + p_\mathrm{LZ}(\Omega_\mathrm{D}, \alpha_\mathrm{D}) \\ & - 2p_\mathrm{LZ}(\Omega_\mathrm{G}, \alpha_\mathrm{G})\, p_\mathrm{LZ}(\Omega_\mathrm{D}, \alpha_\mathrm{D}). \end{aligned}$$

The probability that the two-level system emits a photon following the two-pulse combination is P_1. The probability that the photon is detected is the point spread function of the detection channel, a Gaussian function centred at $(x, y) = (0, 0)$ (the square of eq. 4a), multiplied by a constant factor β, the efficiency of the entire microscope–detector system. We arrive at an analytical result for the imaging signal:

$$\begin{aligned} \mathrm{RF}(x, y) =& \beta\, P_1(\Omega_\mathrm{G}, \alpha_\mathrm{G}, \Omega_\mathrm{D}, \alpha_\mathrm{D}) \\ & \cdot \exp\left(-\frac{k^2\sigma^2(x^2 + y^2)}{f^2}\right). \end{aligned} \tag{6}$$

The RF function is plotted in Fig. S9 as a function of (x, y) for three different values of Ω_G^0 and three different values of Ω_D^0. For large Ω_G^0, a bright spot appears at $(x, y) = (0, 0)$ whose width decreases as Ω_D^0 increases: this describes the main modus operandi of the imaging

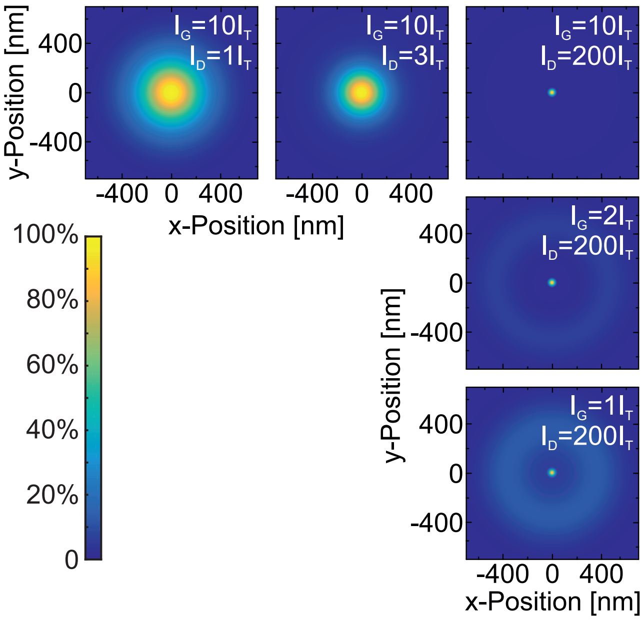

FIG. S9. **Calculated images.** The function RF(x, y), eq. 6, is plotted for $\lambda = 940\,\text{nm}$, $n_{\text{SIL}} = 2.13$, $\Delta X_{I,\text{FWHM}} = 2.0\,\text{mm}$ ($\sigma = 1.2\,\text{mm}$), $f = 5.9\,\text{mm}$, $\alpha_{\text{G}} = -\alpha_{\text{D}} = 3.24\,\text{ps}^{-2}$. For large Gauss beam intensity, the central spot decreases in size retaining the maximum signal as the doughnut beam intensity increases. For large doughnut beam intensity, a ring surrounds the central spot at small Gauss beam intensity. The ring weakens and moves to larger radii as the Gauss beam intensity increases.

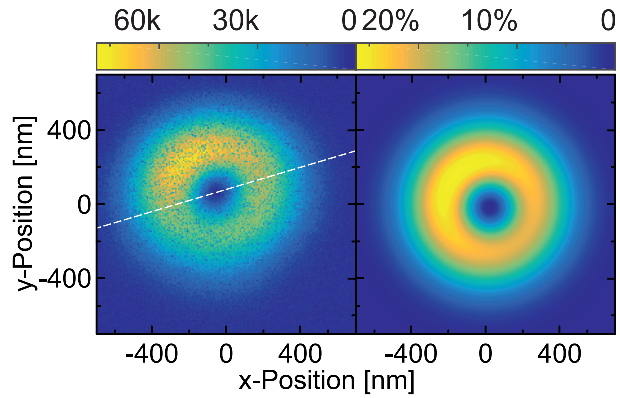

FIG. S10. **Doughnut beam displacement.** Left: Resonance fluorescence from quantum dot QD01 measured with the doughnut-shaped pulse alone and left circularly polarized excitation. The excitation intensity was $I_D^0 = 1.2 I_T$. A cut along the white dashed line is plotted in Fig. S5. Right: corresponding simulation with $I_D^0 = 1.2 I_T$, parameters as stated in Fig. S9 and a displacement of $\Delta x_D = 20\,\text{nm}$ and $\Delta y_D = -20\,\text{nm}$.

scheme. At intermediate Ω_{G}^0, a ring appears surrounding the central maximum. The ring appears at locations where the Gauss beam leaves part of the population in state $|0\rangle$, and the doughnut beam transfers part of this population into state $|1\rangle$, resulting in a weak residual signal. As Ω_{G}^0 increases the ring moves to larger radii in the focal plane and it weakens: it can be suppressed in practice simply by choosing a large enough Gauss beam intensity.

In the limit of large Ω_{G}^0 and Ω_{D}^0, it is possible to derive a result for the FWHM of the central maximum, Δx_{FWHM}. We assume that Ω_{G}^0 is large enough such that $p_{\text{LZ}}(\Omega_{\text{G}}) \simeq 0$ over the central bright spot. Expanding the doughnut field $E_{\text{D}}(x, y)$ as a Taylor series in (x, y) and retaining only the linear term, we find

$$\Delta x_{\text{FWHM}} = \frac{\Delta x_{I,\text{FWHM}}^0}{\sqrt{1 + \frac{\pi^2 (\Omega_{\text{D}}^0)^2}{16\alpha}}} = \frac{\Delta x_{I,\text{FWHM}}^0}{\sqrt{1 + (\Omega_{\text{D}}^0/\Omega_{\text{T}})^2}}.$$

This has the same dependence on the doughnut beam intensity as the STED protocol[17,18]. We define here a characteristic Rabi frequency, $\Omega_T = 4\sqrt{\alpha}/\pi$ corresponding to a pulse area of $\Theta(\Omega_{\text{T}}) = \sqrt{32/\pi} \approx 1.02\pi$ and hence an occupation probability of $\sim$92 % (using eq. 5) following excitation with a single RAP pulse. We transform the Rabi frequencies into intensities with $I = \frac{1}{2} c \epsilon_0 n (\hbar\Omega)^2/\mu_{01}^2$:

$$\Delta x_{I,\text{FWHM}} = \frac{\Delta x_{I,\text{FWHM}}}{\sqrt{1 + \frac{I_{\text{D}}^0}{I_{\text{T}}}}},$$

$$I_{\text{T}} = \frac{8\alpha\hbar^2 c\epsilon_0 n}{\pi^2 \mu_{01}^2},$$

with c the speed of light, n the refractive index and ϵ_0 the vacuum permittivity.

As a final point, we note that the response to the doughnut beam alone can exhibit a radial asymmetry, Fig. S10. This arises as a consequence of a small displacement of the doughnut zero with respect to the collection point spread function. By introducing a small displacement in the model, we can reproduce the experimental results convincingly, Fig. S10. Likewise, the ring in the calculated RF(x, y) function for intermediate Ω_{G}^0 also becomes radially asymmetric in the presence of this displacement. However, in the main imaging regime, the central bright spot lies at the central zero of the doughnut beam and is only very weakly influenced by a lateral displacement of the Gauss beam, equivalently the collection point spread function. The main experimental requirement is therefore to create a high quality doughnut beam.

[1] Prechtel, J. H. *et al.* Decoupling a hole spin qubit from the nuclear spins. *Nat. Mater.* **15**, 981–986 (2016).

[2] Warburton, R. J. *et al.* Optical emission from a charge-tunable quantum ring. *Nature* **405**, 926–929 (2000).

[3] Dalgarno, P. A. *et al.* Coulomb interactions in single charged self-assembled quantum dots: Radiative lifetime and recombination energy. *Phys. Rev. B* **77**, 245311 (2008).

[4] Warburton, R. J. Single spins in self-assembled quantum dots. *Nat. Mater.* **12**, 483–493 (2013).

[5] Kurzmann, A., Ludwig, A., Wieck, A. D., Lorke, A. & Geller, M. Auger recombination in self-assembled quantum dots: quenching

and broadening of the charged exciton transition. *Nano Lett.* **16**, 3367–3372 (2016).

[6] Kuhlmann, A. V. *et al.* Charge noise and spin noise in a semiconductor quantum device. *Nat. Phys.* **9**, 570–575 (2013).

[7] Kuhlmann, A. V. *et al.* A dark-field microscope for background-free detection of resonance fluorescence from single semiconductor quantum dots operating in a set-and-forget mode. *Rev. Sci. Instrum.* **84**, 073905 (2013).

[8] Weiner, A. M., Leaird, D. E., Patel, J. S. & Wullert, J. R. Programmable shaping of femtosecond optical pulses by use of 128-element liquid crystal phase modulator. *IEEE J. Quantum Electron.* **28**, 908–920 (1992).

[9] Martinez, O. 3000 times grating compressor with positive group velocity dispersion: Application to fiber compensation in 1.3-1.6 μm region. *IEEE J. Quantum Electron.* **23**, 59–64 (1987).

[10] Weiner, A. M. *Ultrafast Optics* (Wiley, Hoboken, N.J, 2009).

[11] Hao, X., Kuang, C., Wang, T. & Liu, X. Effects of polarization on the de-excitation dark focal spot in STED microscopy. *J. Opt.* **12**, 115707 (2010).

[12] Neupane, B., Chen, F., Sun, W., Chiu, D. T. & Wang, G. Tuning donut profile for spatial resolution in stimulated emission depletion microscopy. *Rev. Sci. Instrum.* **84**, 043701 (2013).

[13] Bokor, N., Iketaki, Y., Watanabe, T. & Fujii, M. Investigation of polarization effects for high-numerical-aperture first-order Laguerre-Gaussian beams by 2D scanning with a single fluorescent microbead. *Opt. Express* **13**, 10440 (2005).

[14] Landau, L. On the theory of transfer of energy at collisions II. *Phys. Z. Sowjetunion* **2**, 46 (1932).

[15] Zener, C. Non-adiabatic crossing of energy levels. *Proc. R. Soc. A Math. Phys. Eng. Sci.* **137**, 696–702 (1932).

[16] Simon, C.-M. *et al.* Robust quantum dot exciton generation via adiabatic passage with frequency-swept optical pulses. *Phys. Rev. Lett.* **106**, 166801 (2011).

[17] Westphal, V. & Hell, S. W. Nanoscale Resolution in the Focal Plane of an Optical Microscope. *Phys. Rev. Lett.* **94**, 143903 (2005).

[18] Harke, B. *et al.* Resolution scaling in STED microscopy. *Opt. Express* **16**, 4154–4162 (2008).